Available online at www.sciencedirect.com
ScienceDirect
Trans. Nonferrous Met. Soc. China 31(2021) 3075−3086
Transactions of Nonferrous Metals Society of China
www.tnmsc.cn

Microstructure and properties of biodegradable co-continuous (HA+β-TCP)/Zn−3Sn composite fabricated by vacuum casting-infiltration technique

Ting-liang YAN, Xiang WANG, Jin-long FAN, Qi-dong NIE

Key Laboratory of Superlight Material and Surface Technology, Ministry of Education, Harbin Engineering University, Harbin 150001, China

Received 28 November 2020; accepted 18 June 2021

Abstract: The co-continuous (HA+β-TCP)/Zn−3Sn composite was fabricated via vacuum casting-infiltration method. The microstructure, mechanical properties, corrosion behaviors, and hemolysis ratio of the composite were studied by scanning electron microscope, X-ray diffractometer, mechanical testing, electrochemical test, immersion test, and ultraviolet spectrophotometry. The results indicate that Zn−3Sn alloy infiltrated into porous HA+β-TCP scaffold, which resulted in the formation of a compact (HA+β-TCP)/Zn−3Sn co-continuous composite, without any reaction layer between the Zn−3Sn alloy and the HA+β-TCP scaffold. The compressive strength of the composite was equal to about 3/4 that of Zn−3Sn alloy bulk. The corrosion rate of composite in simulated body fluid solution was slightly higher than that of Zn−3Sn alloy bulk. The main corrosion product on the composite surface was $Zn(OH)_2$. The hemolysis rate of the composite was lower than that of Zn–3Sn alloy bulk and exhibited superior blood compatibility.

Key words: co-continuous (HA+β-TCP)/Zn−3Sn composite; microstructure; mechanical properties; corrosion behavior; hemolysis rate

1 Introduction

In the past decade, temporary implanted biodegradable metals have attracted significant research interests due to their excellent biocompatibility and promising mechanical properties. Biodegradable implants provide mechanical support during the tissue repair period and then undergo gradual degradation in the physiological environment [1,2]. Current studies on biodegradable implants mostly focus on the following three alloying systems: Mg-based, Fe-based, and Zn-based alloys. Mg-based alloys, such as Mg−Ca [3], Mg−Zn [4], Mg−Zn−Mn−Sr [5], Mg−Sn [6], AZ91, and AZ31 alloys [7], are the mostly reported alloy systems; however, the key difficulty in achievement of their low degradation rate in the body fluid environment is a main problem for the extensive clinical application of these alloys [8,9]. Literature studies about Fe-based biodegradable materials, such as Fe−Mn [10], Fe−Mg [11], Fe/β-tricalcium phosphate (β-TCP) [12], and Fe/Mg_2Si [13], indicate that the low degradation rate and the lack of bioactivity and osteoconductivity are the significant factors hindering their wide-spread use [14]. Some methods have been proposed to eliminate above-mentioned problems; nonetheless, till date very limited improvement has been achieved. In contrast, the electrode potential of Zn is in the middle of those of Mg and Fe, which have moderate degradation rate [15]. Furthermore, as an essential nutrient, Zn possesses many important biological

Corresponding author: Xiang WANG, Tel: +86-451-82569890, E-mail: wangxiang@hrbeu.edu.cn
DOI: 10.1016/S1003-6326(21)65716-3

functions, including cell differentiation and growth and nervous system immunity [16]. Moreover, Zn can also promote the bone formation by improving osteoblast differentiation and activity whilst simultaneously inhibiting osteoclastogenesis and resorption [17−19]. Recently, a set of binary and ternary biodegradable Zn-based alloys, such as Zn−Mg [20,21], Zn−Mn [22], Zn−Ca [23], Zn−Cu [24], Zn−Cu−Mg [25], Zn−Mg−Fe [26], Zn−Mg−Mn [27], and Zn−Mg−Sr [28] have been proposed and fabricated to fulfill their functions as biomedical implants. These alloys exhibit sound strength; however, the degradation rate is too low to satisfy the biomedical requirements. On the other hand, the pharmacological performance of Zn ions is significantly dependent on the release process. In general, the initial burst release of Zn ion in the body may induce adverse reactions. Thus, systematic control of the release process is required, and a slow and sustained rate is necessary through the process of bone tissue regeneration. Moreover, a further improvement in the biocompatibility is a critical factor for Zn-based alloys to be widely used in the field of medical health.

Till date, some significant research efforts have been devoted to obtaining the required degradation rate and biocompatibility of the Zn-based alloys, and development of new alloy or composite is one of the promising methods [29,30]. For instance, MIAO et al [29] fabricated a new biphasic ZnTCP/FHA layer on titanium alloy substrate. The results showed that ZnTCP could extend release of Zn ions in a much longer period for up to 10 d. Furthermore, the ZnTCP/FHA layer showed a statistically significant increase in cell viability compared to the corresponding biphasic TCP/FHA layer without Zn. In the previous research study [31], a co-continuous (β-TCP+ MgO)/Zn−Mg composite was fabricated by suction exsorption technique. The (β-TCP+MgO)/Zn−Mg composite showed excellent mechanical properties and corrosion resistance, which were found to be superior compared to other biomaterials. One of the promising methods for improving the release ability of Zn-based alloys is to fabricate new composite, which should be reinforced with bioceramic material with natural human bone compositions such as hydroxylapatite (HA) and β-TCP. Moreover, the interpenetrating bio-composites with porous ceramic or porous nonmetal/metal have special structures and good fascinating properties, which are beneficial to fabricating the implant materials [32,33]. The main advantages of these composites include the improved mechanical properties and adjustable biodegradation rate for bone tissue ingrowth. The composite exhibited different biodegradation rates in its continuous networks. The bone tissue was expected to grow toward the fastest biodegrading network, while the remaining networks still maintained their geometrical shape and carried the physiological load for the tissue ingrowth.

Furthermore, several studies have reported the superiority of osteoinduction of implanted BCP (HA+β-TCP) bioceramics over pure HA and pure β-TCP, respectively. The BCP containing 20% HA and 80% β-TCP was found to be the best [34]. On the other hand, Sn is one of the non-toxic and necessary elements in the human body [35], thus herein Sn was embraced as an alloying element to improve the mechanical properties and corrosion performance of Zn alloy. However, as far as we know, very limited research effort has been devoted to the study on the biodegradable Zn−Sn alloy. KUBÁSEK et al [6] reported that Mg−Sn alloys exhibited appropriate mechanical properties and good biocompatibility. In Ref. [36], (HA+β-TCP)/Mg−5Sn composite was characterized and evaluated. The results showed that (HA+β-TCP)/Mg−5Sn interpenetrating composite exhibited appropriate mechanical and corrosion properties, which made it a potential candidate material for bone repair. Therefore, due to the biocompatibility of Sn, it was speculated that alloying Zn with Sn could present new biodegradable alloy with desirable performance.

In this study, a new co-continuous (HA+β-TCP)/Zn−3Sn composite was prepared using Zn−3Sn alloy and HA+β-TCP scaffold as continuous phases, respectively. The microstructure, mechanical properties, corrosion behavior, and hemolytic property were studied systematically to evaluate its feasibility as structural material for biodegradable implant.

2 Experimental

2.1 Materials preparation

The process of fabrication of (HA+β-TCP)/Zn−3Sn composite involves the following three

steps: preparation of porous HA+*β*-TCP scaffold, Zn−3wt.%Sn alloy (expressed as Zn−3Sn alloy in the remaining part of the paper), and vacuum casting-infiltration of molten Zn–3Sn alloy into the porous scaffold. Commercial thermoplastic polyurethane (PU, 40 ppi) foam was used as a template to prepare porous HA+*β*-TCP. Pretreatment of PU foam and fabrication and adhesion of ceramic slurry were described in Ref. [37]. The ceramic powder was the mixture of HA powder (average particle size of 2 μm) and *β*-TCP powder (average particle size of 2.5 μm), and the HA/*β*-TCP mass ratio was 20/80. The ceramic slurry-coated PU foams were dried at 60 °C in a drying oven for at least 24 h. Then, they were heated to 600 °C at a heating rate of 0.6 °C/min for pyrolysis of the PU foam in a furnace, which was followed by heat treatment at 1100 °C for 4 h to prepare porous HA+*β*-TCP. Subsequently, the furnace was cooled down to room temperature at a cooling rate of 5 °C/min. Finally, each porous HA+*β*-TCP scaffold was removed, weighed, and kept in a desiccator.

Zn−3Sn alloy was prepared by melting high-purity Zn and Sn ingots (purity > 99.9%) in an electrical resistance furnace at 530 °C under shielding gas atmosphere of SF_6+CO_2. Molten alloy was mechanically agitated for 2 min to enhance the alloy melt homogeneity. The co-continuous (HA+*β*-TCP)/Zn−3Sn composite was prepared by infiltrating the molten Zn−3Sn alloy into the porous HA+*β*-TCP scaffold using a self-made vacuum casting-infiltration equipment, and the specific fabrication equipment was described in Ref. [31]. During the fabrication process, the porous HA+*β*-TCP was preheated at 150 °C and placed in the vacuum casting-infiltration equipment. Then, the molten Zn−3Sn alloy was poured at (510±5) °C into the HA+*β*-TCP scaffold, the equipment was vacuumized to −0.08 to −0.06 MPa simultaneously, and this pressure was maintained for about 4 min to ensure the infiltration of the liquid metal. Finally, the pressure was released after the complete solidification of the melt and the (HA+*β*-TCP)/Zn−3Sn composite was removed from the vacuum casting-infiltration equipment. Zn−3Sn alloy bulk prepared by the above-mentioned vacuum casting-infiltration method was used as reference for comparative analysis.

2.2 Microstructure characterization

The constituent phases of Zn−3Sn alloy bulk, (HA+*β*-TCP)/Zn−3Sn composite, and their corrosion products were identified by X-ray diffraction (XRD) with Cu K_α radiation at the step size of 0.02° and a scan rate of 2 (°)/min. The microstructures of the porous HA+*β*-TCP and the (HA+*β*-TCP)/Zn−3Sn composite were investigated by scanning electron microscopy (SEM) combined with energy dispersive spectrometry (EDS).

2.3 Compressive test

The uniaxial compressive tests were conducted at a constant nominal strain rate of 7×10^{-4} s^{-1} in accordance with ASTM E9—89a (2000) standard using a universal material test machine (Instron 3365). The samples were machined into rectangular solid with dimensions of 3 mm × 3 mm × 6 mm. Five specimens were tested in parallel for each group.

2.4 Electrochemical test

The potentiodynamic polarization test was conducted with an electrochemical workstation (SI1287) at a temperature of (37±0.5) °C in simulated body fluid (SBF). A traditional three-electrode cell was used for electrochemical measurement. A platinum foil and a saturated calomel electrode were used as the counter electrode and the reference electrode, respectively. The specimen with an exposed area of 1 cm^2 was used as the working electrode. The potentiodynamic polarization test was performed at a scanning rate of 1 mV/s. Three samples were tested for each group. The chemical composition (ions concentration in mmol/L) of the standard SBF solution was: 142.0 Na^+, 5.0 K^+, 1.0 Mg^{2+}, 2.5 Ca^{2+}, 109.0 Cl^-, 27.0 HCO_3^-, 1.0 HPO_4^{2-}, and 1.0 SO_4^{2-} [38]. The pH of the SBF was adjusted to 7.4 using HCl and tris(hydroxy-methyl) aminomethane.

2.5 Immersion test

The immersion test was performed using samples with dimensions of 5 mm × 5 mm × 8 mm. The immersion test was carried out in SBF solution at (37±0.5) °C according to ASTM-G31 — 72 standard [39]. The pH of the solution was recorded during the immersion test at an interval of 1 d. Zn^{2+} concentration in the SBF solution was determined

by inductively coupled plasma atomic emission spectrometry (ICP-AES, 5300 DV). The samples were removed from SBF solution after different immersion periods, then gently rinsed with distilled water, and finally dried at room temperature. XRD was used to characterize the corrosion products formed on the exposed surface of samples. The so-formed corrosion products were removed using chromic acid (CrO_3) solution before performing the morphological analysis by SEM. Cleaned samples were then reweighed using an electronic balance with a measuring sensitivity of 0.1 mg to determine their mass loss during immersion in SBF solution for 15 d. An average of five measurements was taken for each group. The corrosion rate was calculated according to the following equation:

$$C_R=K\Delta w/(\rho At) \quad (1)$$

where C_R is the corrosion rate (mm/a), K is a constant that equals 87.6, Δw is the mass loss (mg), ρ is the density of sample (g/cm^3), A is the initial sample area exposed to solution (cm^2), and t is the immersion time (h) [1].

2.6 Hemolysis test

Human blood from a healthy volunteer was mixed with sodium citrate (3.8 wt.%) in the ratio of 9:1 and then diluted with physiological saline in a volume ratio of 4:5. Samples were then dipped in centrifuge tubes containing physiological saline (10 mL) and incubated at (37±0.5) °C for 30 min. Then, diluted blood (0.2 mL) was added to these tubes and the mixtures were incubated at (37±0.5) °C for 60 min. Thereafter, the samples were removed and all the mixture solutions were centrifuged at 1500 r/min for 5 min. The supernatant from each tube was transferred to a cuvette where the absorbance was measured using an ultraviolet (UV) spectrophotometer at 545 nm. The normal saline solution and deionized water were used as a negative control and a positive control, respectively. An average of three measurements was taken for each group. The hemolysis ratio was calculated as follows:

$$H_R=(D_t-D_{nc})/(D_{pc}-D_{nc})\times 100\% \quad (2)$$

where H_R is hemolysis ratio; D_t, D_{nc}, and D_{pc} are absorbances of sample, negative control, and positive control, respectively.

3 Results and discussion

3.1 Microstructure and mechanical properties

Figure 1(a) exhibits the structure of porous HA+β-TCP scaffold obtained by replicating the PU foam. The porous HA+β-TCP showed a three-dimensional network structure, and the porosity was 88% (determined by following the method described in Ref. [36]). The diameter of pores ranged from 400 to 600 μm. The porous structure of HA+β-TCP scaffold is beneficial to the infiltration of molten metal. On the other hand, some micropores and voids were also formed in the struts due to the burning out of PU sponge during the pyrolysis process. Figure 1(b) shows SEM image of the co-continuous (HA+β-TCP)/ Zn−3Sn composite. The dark, gray, and brilliant regions correspond to HA+β-TCP scaffold, α-Zn, and β-Sn, respectively. The results indicate that (HA+β-TCP)/ Zn−3Sn composite consisted of a closed-cell and compact structure. Furthermore, the interface between Zn−3Sn alloy and HA+β-TCP scaffold was

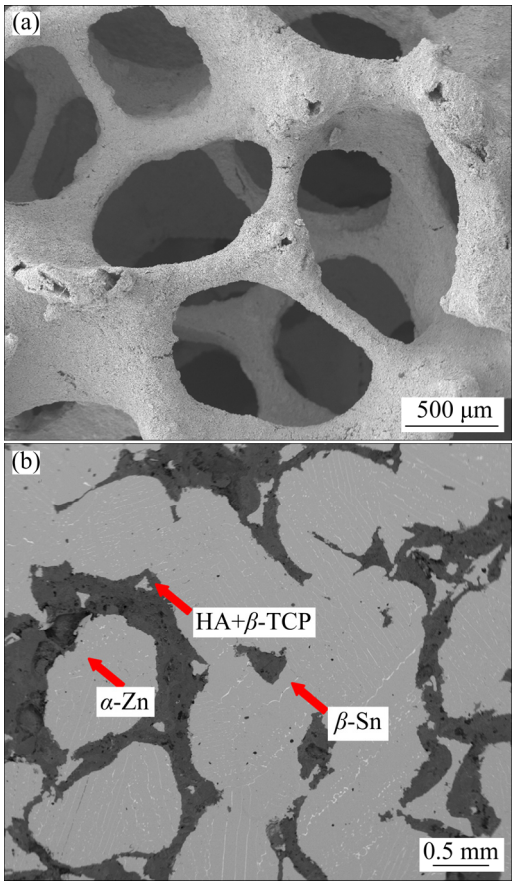

Fig. 1 SEM images of porous HA+β-TCP (a) and (HA+β-TCP)/Zn−3Sn composite (b)

smooth and the co-continuous networks were still clear. Besides, the micropores and voids in the struts of the original HA+β-TCP scaffold were also filled with Zn−3Sn alloy. As a result, the volume fraction of HA+β-TCP in (HA+β-TCP)/Zn−3Sn composite was about 12%.

Figure 2 demonstrates the interface microstructure and EDS analysis of (HA+β-TCP)/Zn−3Sn composite. There was no obvious gap or discernible debonding at the interface between Zn–3Sn alloy and HA+β-TCP, which indicates good integration of interfaces, as shown in Fig. 2(a). Comparison of Figs. 2(e) and (f) with Fig. 2(a) reveals the existence of Zn and Sn elements in the pores, and the micropores and voids in the struts of HA+β-TCP scaffold, indicating that the molten Zn−3Sn alloy penetrated not only the pores, but also the micropores and voids in the struts of the HA+β-TCP scaffold. The compact structure of (HA+β-TCP)/Zn−3Sn composite also demonstrated that the effective infiltration of liquid alloy into the porous scaffold was realized via vacuum casting-infiltration method. Moreover, it was proved in Ref. [31] that the compact composite with interconnected network structure could be realized by suction exsorption technique. In general, the compact structure of the (HA+β-TCP)/Zn−3Sn composite fabricated by vacuum casting-infiltration technique could be attributed to the following two factors: (1) the good wettability of β-TCP and Zn [40], and (2) the gravity of Zn−3Sn matrix alloy and the external pressure exerted by the vacuum casting-infiltration equipment during the process of infiltration and solidification.

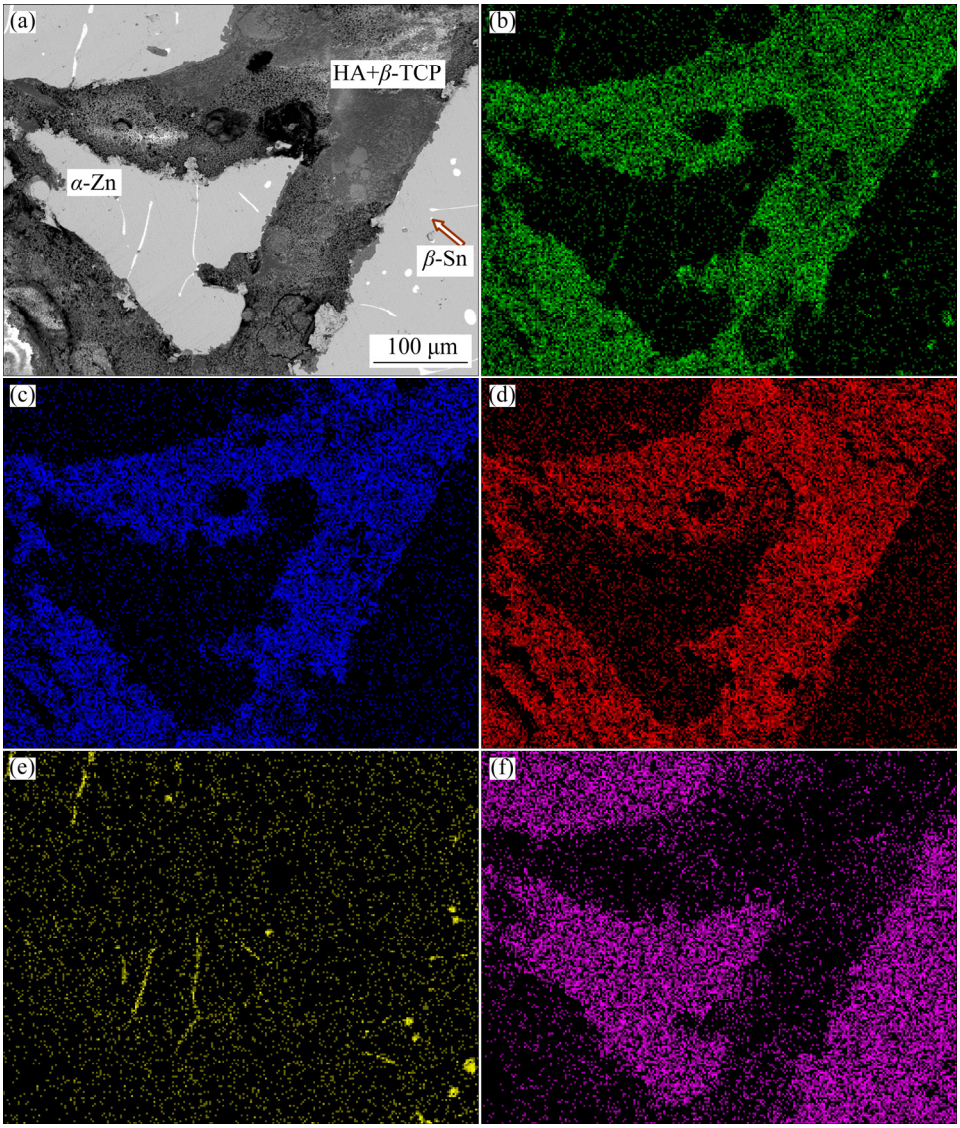

Fig. 2 Interface microstructure (a) and EDS elemental mapping (b−f) of (HA+β-TCP)/Zn−3Sn composite: (a) SEM image; (b) Ca; (c) P; (d) O; (e) Sn; (f) Zn

Figure 3 shows the XRD patterns of Zn−3Sn alloy bulk and (HA+β-TCP)/Zn−3Sn composite. The XRD result indicated that both the alloy bulk and composite were mainly composed of α-Zn and β-Sn phases. Moreover, a small amount of β-TCP and HA phases were also found in the composite. Furthermore, no other new phases were detected, indicating that there was no any interaction between Zn−3Sn alloy and HA+β-TCP scaffold.

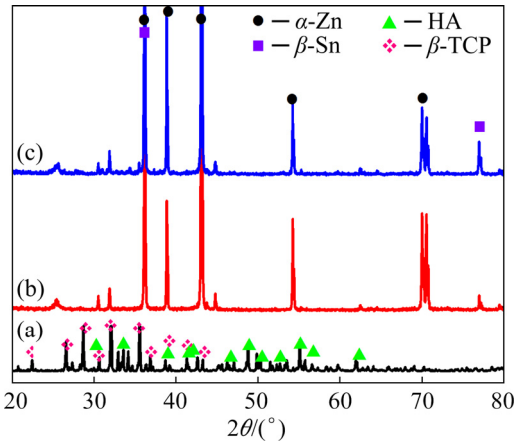

Fig. 3 XRD patterns of porous HA+β-TCP (a), Zn−3Sn alloy bulk (b) and (HA+β-TCP)/Zn−3Sn composite (c)

The representative compression stress–strain curves of (HA+β-TCP)/Zn−3Sn composite and Zn−3Sn alloy bulk are presented in Fig. 4. The results indicated that the composite exhibited a compressive strength of 115 MPa, approximately 3/4 that of Zn−3Sn alloy bulk (159 MPa), and was far higher than that of the sintered HA+β-TCP ceramic bulk (about 8.47 MPa) [41]. In order to evaluate the strength of the (HA+β-TCP)/Zn−3Sn composite prepared in this study, the comparison of compressive strength was performed among Zn alloy bulk, composites, and human bone, and the corresponding results are summarized in Table 1. The results demonstrated that the compressive strength of (HA+β-TCP)/Zn−3Sn composite was comparable to that of the human bone. Apparently, the continuously distributed HA+β-TCP in Zn−3Sn matrix acts as brittle phase and reduces the compressive strength of the composite. It is believed that the interpenetration of metal stabilizes the porous ceramic struts and partially hinders cracks initiation and growth. Thus, an excellent interlocking structure is formed in the composite that stiffens the interface between matrix and improvement phases. This results in a higher compressive strength of the composite compared to that of the porous scaffold [43]. Although the interfacial combination was good in (HA+β-TCP)/Zn−3Sn composite (as shown in Fig. 1(b)) and the hollow structure of HA+β-TCP scaffold was completely filled with Zn−3Sn alloy (as shown in Fig. 2(a)), the co-continuous brittle HA+β-TCP structure led to the decrease of compressive strength. Therefore, the compressive strength of the co-continuous (HA+β-TCP)/Zn−3Sn composite was slightly lower than that of Zn−3Sn alloy bulk.

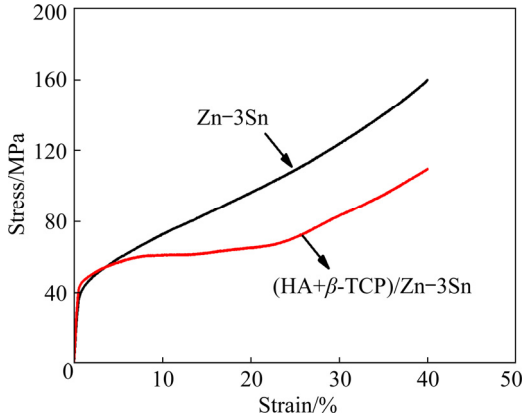

Fig. 4 Compressive behaviors of (HA+β-TCP)/Zn−3Sn composite and Zn−3Sn alloy bulk

Table 1 Compressive strength of Zn alloy bulk and composites in comparison with strengths of human bone

Materials	Compressive strength/MPa	Ref.
Zn−1Mg	350	[31]
Zn−4Mn	290	[22]
(β-TCP+MgO)/Zn−Mg composite	244	[31]
Cortical bone	130−180	[42]
Femur	167	[42]
Tibia	159	[42]

3.2 Electrochemical behavior

Figure 5 displays potentiodynamic polarization curves of (HA+β-TCP)/Zn−3Sn composite, with Zn−3Sn alloy bulk as the control. The corrosion potential of (HA+β-TCP)/Zn−3Sn composite was −1.06 V, which is slightly less (~10 mV) than that of Zn−3Sn alloy bulk. Moreover, the corrosion current density (J_{corr}) calculated from the potentiodynamic polarization curves indicates that J_{corr} value of (HA+β-TCP)/Zn−3Sn composite was ~64% higher than that of Zn−3Sn alloy bulk, i.e.,

33.7 μA/cm^2 against 20.6 μA/cm^2, respectively. It can be inferred from the above-mentioned results that the corrosion behavior of the composite was slightly improved compared to that of Zn−3Sn alloy bulk.

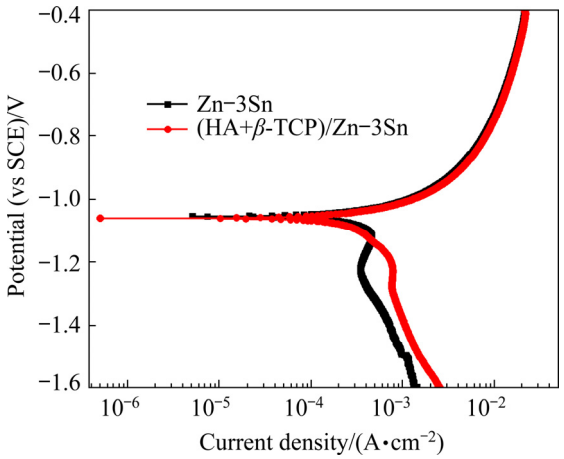

Fig. 5 Potentiodynamic polarization curves of (HA+β-TCP)/Zn−3Sn composite in SBF, with Zn−3Sn alloy bulk as control

3.3 Immersion test results

The pH variation of the SBF solution incubating Zn−3Sn alloy bulk and (HA+β-TCP)/Zn−3Sn composite as a function of immersion time is shown in Fig. 6. Clearly, the pH of SBF solutions with (HA+β-TCP)/Zn−3Sn composite and Zn−3Sn alloy bulk exhibited similar change tendency with the immersion duration. During the entire immersion process, the pH of SBF solution with the composite was higher than the value with the alloy bulk; however, the increasing amplitude was not more than 0.42. The pH of SBF solution with the composite tended to increase during the first day of immersion due to the formation of significant amount of OH^- ions, jumping from original 7.4 to 7.8, and then decreased slowly and stabilized at about 7.6 after immersion for up to 8 d.

The dissolution of Zn in (HA+β-TCP)/Zn−3Sn composite was evaluated based on ICP-AES analysis by immersing the composite in SBF solution. Figure 7 presents Zn^{2+} concentration of the SBF solution after immersion of (HA+β-TCP)/Zn−3Sn composite and Zn−3Sn alloy bulk for 3, 7, and 15 d, respectively. Clearly, the released Zn^{2+} concentration increased with increasing immersion time. In initial immersion period (3 d and 7 d), the released Zn^{2+} concentration from the composite was slightly lower than that from Zn−3Sn alloy bulk;

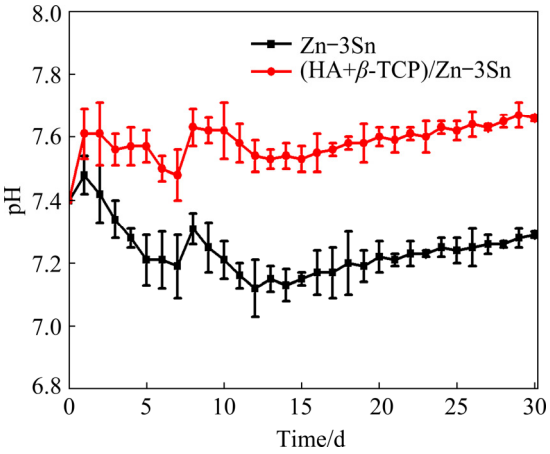

Fig. 6 pH values of SBF solution incubating Zn−3Sn alloy bulk and (HA+β-TCP)/Zn−3Sn composite at different immersion time

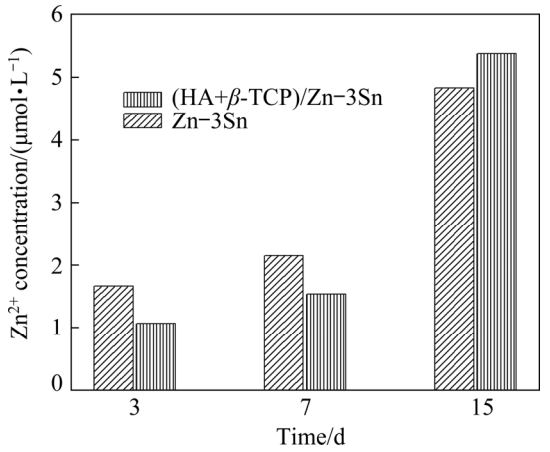

Fig. 7 Zn^{2+} concentration of SBF solutions after immersion of Zn−3Sn alloy bulk and (HA+β-TCP)/Zn−3Sn composite for 3, 7 and 15 d

however, after 15 d of immersion, more Zn^{2+} was released from the composite. The released Zn^{2+} concentration also showed that the degradation rate of the composite was improved compared to that of Zn−3Sn alloy bulk during the initial immersion period. Interestingly, no "burst" release of Zn^{2+} was observed from both the composite and Zn−3Sn alloy bulk. The Zn^{2+} release process was sustained for up to 15 d and was less than the Zn^{2+} concentration at normal blood serum level of 12.4−17.4 μmol/L [44]. Recently, CHENG et al [45] have reported that 15 μmol/L Zn was not toxic to ECV304 cells. Therefore, ICP-AES results revealed that (HA+β-TCP)/Zn−3Sn composite provided a continuous Zn^{2+} release platform and benefited to the bone repairing. In addition to the Zn^{2+} release, the dissolution of HA+β-TCP after implantation can

cause an increase in the local concentrations of Ca^{2+} and PO_4^{3-}, thereby facilitating the subsequent mineralization process, which is a crucial step in the bone formation process [29].

The corrosion rates after immersion in SBF solution at (37±0.5) °C for 15 d were 0.26 mm/a for the composite and 0.02 mm/a for Zn−3Sn alloy bulk. Similarly, the Zn^{2+} concentration released into SBF solution during the exposure period showed that the composite exhibited the higher value (5.37 μmol/L) compared to Zn–3Sn alloy bulk (4.83 μmol/L), as shown in Fig. 7, which indicated a good correlation between these two results because low release of metal ions could be attributed to lower corrosion rate. It showed that Zn−3Sn alloy could be degraded in SBF solution, in particular, with HA+*β*-TCP scaffold addition; moreover, it was also found that the addition of HA+*β*-TCP scaffold enhanced the corrosion rate of the composite. This indicated that the corrosion behavior of the composite was improved compared to Zn−3Sn alloy bulk. Furthermore, it was confirmed that the corrosion rate of the studied composite was lower than that of the mostly reported Mg-based alloys for biomedical applications, and was higher than that of the degradable Fe-based and Zn-based alloys, and was close to the expected data (0.2 mm/a) as a promising biodegradable material [21,27]. According to Ref. [46], the typical model of the studied composite implants was assumed to be a cylinder with a diameter of 4 mm and a length of 25 mm. Thus, implants in the body might provide a Zn dose of 1.62 mg/d, which is far below the suggested daily intake of 15 mg/d. Based on this, (HA+*β*-TCP)/Zn–3Sn composite could be considered as a biodegradable material with appropriate corrosion behavior. The difference in corrosion rate between the composite and Zn−3Sn alloy bulk could be explained according to the distribution pattern and morphology of HA+*β*-TCP scaffold in the Zn−3Sn matrix. On the one hand, the interconnected HA+*β*-TCP scaffold showed the lower corrosion resistance than that of Zn−3Sn alloy, as shown in Fig. 8. On the other hand, SEM images presented in Figs. 2(b) and 3 exhibited that some pores and voids inside HA+*β*-TCP scaffold were filled with the Zn−3Sn alloy; however, the extra interfaces thereby could become channels for further penetration of corrosive electrolyte into the scaffold, resulting in the increase in the chance of localized and crevice corrosion besides the commonly occurring uniform corrosion. However, the relatively flat surface morphology indicated that Zn−3Sn matrix alloy exhibited nearly uniform corrosion during immersion.

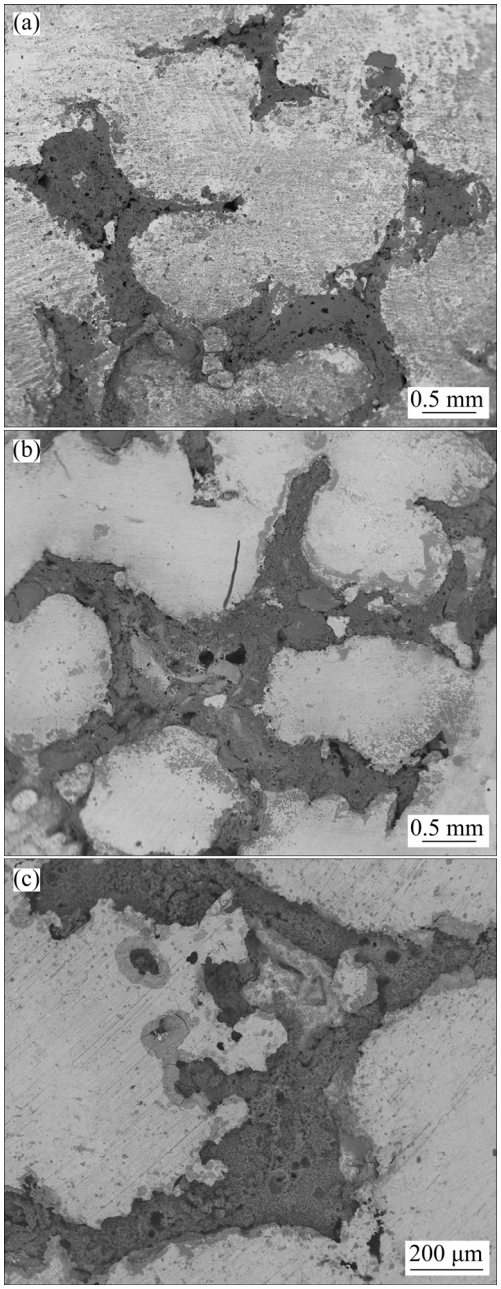

Fig. 8 Morphologies of (HA+*β*-TCP)/Zn−3Sn composite after 3 d (a), 15 d (b) and 30 d (c) immersion in SBF solution

Figure 8 shows the morphologies of (HA+*β*-TCP)/Zn−3Sn composite after 3, 15 and 30 d immersion in SBF solution at (37±0.5) °C. The composite appeared to undergo the localized degradation and the corrosion degree increased with

increasing immersion time. During degradation process, the corrosion pits were fine, shallow, and uniform for Zn−3Sn matrix alloy, which exhibited a uniform corrosion mode macroscopically. However, for the HA+β-TCP scaffold, some holes appeared on the surface after 3 d immersion due to the degradation of Zn−3Sn alloy within it. With the increase in the immersion time, the scaffold became looser, which exhibited progressively more number of pores. The corrosion extent of the HA+β-TCP scaffold aggravated gradually, and slight crevice corrosion along the interface between alloy and the scaffold was also found (Fig. 8(c)). On the other hand, the corroded morphology of the composite indicated that the corrosion rate of the HA+β-TCP scaffold was faster than that of Zn−3Sn matrix alloy. It is reasonable to expect that shortly after the implantation in the bone, the bone tissue grows toward the degradation networks of HA+β-TCP, while the remaining Zn−3Sn alloys still maintain their geometrical shape and carry the physiological load for the tissue ingrowth [32]. XRD results revealed that the main corrosion product on the composite surface was zinc hydroxide ($Zn(OH)_2$), as shown in Fig. 9.

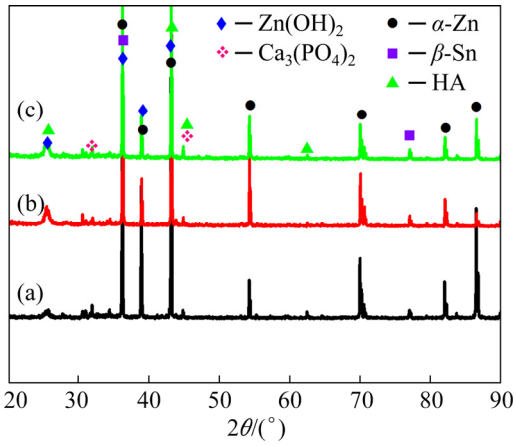

Fig. 9 XRD patterns of (HA+β-TCP)/Zn−3Sn composite after 3 d (a), 15 d (b) and 30 d (c) immersion in SBF solution

After samples were immersed in the SBF solution for 3, 15, and 30 d, respectively, it was observed that the degradation has taken place fairly uniformly over Zn−3Sn matrix surfaces (Fig. 8). When Zn-based alloy is exposed to SBF solution, its corrosion behavior is associated with electrochemical dissolution of Zn occurring according to the following equation [20]:

$$Zn^{2+}+2H_2O=Zn(OH)_2+H_2\uparrow \quad (3)$$

It was reported that the as-generated $Zn(OH)_2$ could form a compact layer, and thus restrain the degradation of Zn alloys and protect Zn substrates [47]. After immersion test, Zn−3Sn matrix showed uniform corrosion surface without any severe local corrosion; however, the corrosion rate of the composite showed a little increasing trend compared to Zn−3Sn alloy bulk, indicating that HA+β-TCP phase may accelerate the corrosion because of its faster degradation rate or crevice corrosion. Figures 8(b) and (c) exhibit the occurrence of slight crevice corrosion along the interface between Zn−3Sn matrix and HA+β-TCP scaffold. In our previous study, occurrence of crevice corrosion was also observed along the interface between Zn−Mg alloy and β-TCP+MgO scaffolds [31]. With the extension in time, the corrosion reactions continued along the interface between Zn−3Sn matrix and HA+β-TCP scaffold, which resulted in the swelling of the composite and allowed the electrolyte to penetrate deeper till the complete breakdown of the composite occurred [48]. Moreover, the stability of $Zn(OH)_2$ film in physiological condition was only temporary. The chloride ions (Cl^-) in SBF solution shifted the passivity region toward the higher pH regions and readily converted $Zn(OH)_2$ to the soluble $ZnCl_2$, thus damaging the protective layer and promoting corrosion [31]. In this way, the formation and the damage of $Zn(OH)_2$ film would cycle until the Zn−3Sn alloy was completely exhausted. In short, the corrosion rate of the composite was determined in terms of the corrosion of HA+β-TCP, Zn−3Sn matrix, and the crevice corrosion.

3.4 Hemolysis property

The hemolysis rates of (HA+β-TCP)/Zn−3Sn composite and Zn–3Sn alloy bulk were 0.40% and 0.53%, respectively, which were far below the recommended value of 5%, a judging criterion for excellent blood compatibility [49]. It was also suggested that the composite showed less destructive effect on erythrocyte compared to the Zn−3Sn alloy bulk. LIU et al [28] also found that pure Zn and Zn−Mg−Sr alloys exhibited good hemocompatibility.

Besides the appropriate mechanical properties of the composite, both the corrosion and hemolytic

properties indicated that (HA+β-TCP)/Zn−3Sn composite showed great potential application in the area of biodegradable implants, as it can guarantee the sufficient mechanical support and the biosafety during the tissue repair process.

4 Conclusions

(1) (HA+β-TCP)/Zn−3Sn composite for biodegradable bone implant material was successfully fabricated by vacuum casting-infiltration technique.

(2) (HA+β-TCP)/Zn−3Sn composite showed compact and co-continuous structure. The ultimate compressive strength of the composite was 115 MPa, which is about 3/4 that of Zn−3Sn alloy bulk and comparable to that of the human bone.

(3) Compared to Zn−3Sn alloy bulk, improved corrosion behavior was confirmed for (HA+β-TCP)/Zn−3Sn composite by the electrochemical and immersion test. The corrosion rate of the composite in SBF solution was 0.26 mm/a. The main corrosion product on the composite surface was $Zn(OH)_2$. The hemolysis rate of the composite was 0.40%.

(4) Appropriate mechanical, corrosion properties and good blood compatibility of the (HA+β-TCP)/Zn−3Sn composite indicated the possibility as a biodegradable biomaterial for bone implant applications.

Acknowledgments

The authors are grateful for the financial supports from the National Natural Science Foundation of China (No. 51101039), and the Fundamental Research Funds for the Central Universities, China (No. 3072020CFT0702).

References

[1] LIU De-bao, XU Guang-quan, JAMALI S S, ZHAO Yue, CHEN Ming-fang, JURAK T. Fabrication of biodegradable HA/Mg−Zn−Ca composites and the impact of heterogeneous microstructure on mechanical properties, in vitro degradation and cytocompatibility [J]. Bioelectrochemistry, 2019, 129: 106−115.

[2] LI H F, SHI Z Z, WANG L N. Opportunities and challenges of biodegradable Zn-based alloys [J]. Journal of Materials Science and Technology, 2020, 46: 136−138.

[3] BAKHSHESHI-RAD H R, IDRIS M H, ABDUL-KADIR M R A, OURDJINI A, MEDRAJ M, DAROONPARVAR M, HAMZAH E. Mechanical and bio-corrosion properties of quaternary Mg−Ca−Mn−Zn alloys compared with binary Mg−Ca alloys [J]. Materials and Design, 2014, 53: 283−292.

[4] TORABI H, FARAJI G, MASOUMI A. Processing characterization of binary Mg−Zn alloys fabricated by a new powder consolidation combined severe plastic deformation method [J]. Journal of Alloys and Compounds, 2020, 832: 154922.

[5] YU Wei-ming, LI Jing-yuan, LI Jian-xing, WANG Jin, LAI Hui-ying, ZHANG Yuan. Effects of trace Sr on microstructure, mechanical properties and corrosion resistance of Mg−0.2Zn−0.1Mn−xSr biomaterials [J]. Rare Metal Materials and Engineering, 2019, 48: 4016−4025. (in Chinese)

[6] KUBÁSEK J, VOJTĚCH D, LIPOV J, RUML T. Structure, mechanical properties, corrosion behavior and cytotoxicity of biodegradable Mg−X (X=Sn, Ga, In) alloys [J]. Materials Science and Engineering C, 2013, 33: 2421−2432.

[7] WITTE F, KAESE V, HAFERKAMP H, SWITZER E, MEYER-LINDENBERG A, WIRTH C J, WINDHAGEN H. In vivo corrosion of four magnesium alloys and the associated bone response [J]. Biomaterials, 2005, 26: 3557−3563.

[8] SONG Guang-ling, HAPUGODA S, ST-JOHN D. Degradation of the surface appearance of magnesium and its alloys in simulated atmospheric environments [J]. Corrosion Science, 2007, 49: 1245−1265.

[9] JARZEBSKA A, BIEDA M, KAWAŁKO J, ROGAL Ł, KOPROWSKI P, SZTWIERTNIA K, PACHLA W, KULCZYK M. A new approach to plastic deformation of biodegradable zinc alloy with magnesium and its effect on microstructure and mechanical properties [J]. Materials Letters, 2018, 211: 58−61.

[10] LI Han-ning, WANG Ya-nan, PENG Qiu-ming. High degradation rate of Fe−20Mn-based bio-alloys by accumulative cryo-rolling and annealing [J]. Materials Science and Engineering C, 2017, 79: 37−44.

[11] KHAN M M, DEEN K M, SHABIB I, ASSELIN E, HAIDER W. Controlling the dissolution of iron through the development of nanostructured Fe−Mg for biomedical applications [J]. Acta Biomaterialia, 2020, 113: 660−676.

[12] HE Fu-po, QIAN Guo-wen, REN Wei-wei, KE Jin-huan, FAN Pei-rong, SHI Xue-tao, CHENG Yan-ling, WU Shang-hua, DENG Xin, YE Jian-dong. Preparation and characterization of iron/beta-tricalcium phosphate bio-cermets for load-bearing bone substitutes [J]. Ceramics International, 2017, 43: 8348−8355.

[13] SIKORA-JASINSKA M, PATERNOSTER C, MOSTAED E, TOLOUEI R, CASATI R, VEDANI M, MANTOVANI D. Synthesis, mechanical properties and corrosion behavior of powder metallurgy processed Fe/Mg_2Si composites for biodegradable implant applications [J]. Materials Science and Engineering C, 2017, 81: 511−521.

[14] REINDL A, BOROWSKY R, HEIN S B, GEIS-GERSTORFER J, IMGRUND P, PETZOLDT F. Degradation behavior of novel Fe/β-TCP composites produced by powder injection molding for cortical bone replacement [J]. Journal of Materials science, 2014, 49: 8234−8243.

[15] YUE Rui, HUANG Hua, KE Gui-zhou, ZHANG Hua, PEI Jia, XUE Guan-hua, YUAN Guang-yin. Microstructure, mechanical properties and in vitro degradation behavior of novel Zn−Cu−Fe alloys [J]. Materials Characterization, 2017,

134: 114−122.

[16] MURNI N S, DAMBATTA M S, YEAP S K, FROEMMING G R A, HERMAWAN H. Cytotoxicity evaluation of biodegradable Zn−3Mg alloy toward normal human osteoblast cells [J]. Materials Science and Engineering C, 2015, 49: 560−566.

[17] MOONGA B S, DEMPSTER D W. Zinc is a potent inhibitor of osteoclastic bone resorption in vitro [J]. Journal of Bone and Mineral Research, 1995, 10: 453−457.

[18] LAKHKAR N J, LEE I H, KIM H W, SALIH V, WALL I B, KNOWLES J C. Bone formation controlled by biologically relevant inorganic ions: Role and controlled delivery from phosphate-based glasses [J]. Advanced Drug Delivery Reviews, 2013, 65: 405−420.

[19] KALIČANIN B M, NIKOLIĆ R S. Potentiometric stripping analysis of zinc and copper in human teeth and dental materials [J]. Journal of Trace Elements in Medicine and Biology, 2008, 22: 93−99.

[20] VOJTĚCH D, KUBÁSEK J, ŠERÁK J, NOVÁK P. Mechanical and corrosion properties of newly developed biodegradable Zn-based alloys for bone fixation [J]. Acta Biomaterialia, 2011, 7: 3515−3522.

[21] DAMBATTA M S, MURNI N S, IZMAN S, KURNIAWAN D, FROEMMING G R A, HERMAWAN H. In vitro degradation and cell viability assessment of Zn−3Mg alloy for biodegradable bone implants [J]. Journal of Engineering in Medicine, 2015, 229: 335−342.

[22] SOTOUDEH-BAGHA P, KHALEGHPANAH S, SHEIBANI S, KHAKBIZ M, ZAKERI A. Characterization of nanostructured biodegradable Zn−Mn alloy synthesized by mechanical alloying [J]. Journal of Alloys and Compounds, 2018, 35: 1319−1327.

[23] LI Hua-fang, YANG Hong-tao, ZHENG Yu-feng, ZHOU Fei-yu, QIU Ke-jin, WANG Xiang. Design and characterizations of novel biodegradable ternary Zn-based alloys with IIA nutrient alloying elements Mg, Ca and Sr [J]. Materials and Design, 2015, 83: 95−102.

[24] NIU Jia-lin, TANG Zi-bo, HUANG Hua, PEI Jia, ZHANG Hua, YUAN Guang-yin, DING Wen-jiang. Research on a Zn−Cu alloy as a biodegradable material for potential vascular stents application [J]. Materials Science and Engineering C, 2016, 69: 407−413.

[25] TANG Zi-bo, HUANG Hua, NIU Jia-lin, ZHANG Lei, HUANG Hua, PEI Jia, TAN Jin-yun, YUAN Guang-yin. Design and characterizations of novel biodegradable Zn−Cu−Mg alloys for potential biodegradable implants [J]. Materials and Design, 2017, 117: 84−94.

[26] WANG Chang, YU Zhen-tao, CUI Ya-jun, ZHANG Ya-feng, YU Sen, QU Gong-qi, GONG Hai-bo. Processing of a novel Zn alloy micro-tube for biodegradable vascular stent application [J]. Journal of Materials Science and Technology, 2016, 32: 925−929.

[27] LIU Xi-wei, SUN Jian-ke, ZHOU Fei-yu, YANG Ying-hong, CHANG Ren-cao, QIU Ke-jin, PU Zhong-jie, LI Li, ZHENG Yu-feng. Micro-alloying with Mn in Zn−Mg alloy for future biodegradable metals application [J]. Materials and Design, 2016, 94: 95−104.

[28] LIU Xi-wei, SUN Jian-ke, YANG Ying-hong, ZHOU Fei-yu, PU Zhong-jie, LI Li, ZHENG Yu-feng. Microstructure, mechanical properties, in vitro degradation behavior and hemocompatibility of novel Zn−Mg−Sr alloys as biodegradable metals [J]. Materials Letters, 2016, 162: 242−245.

[29] MIAO Shun-dong, CHENG Kui, WENG Wen-jian, DU Pi-yi, SHEN Ge, HAN Gao-rong, YAN Wei-qi, ZHANG San. Fabrication and evaluation of Zn containing fluoridated hydroxyapatite layer with Zn release ability [J]. Acta Biomaterialia, 2008, 4: 441−446.

[30] LU Guo-liang, XU Guang-quan, BOBO H L, LIANG Li, LIU De-bao. Fabrication and properties of a biodegradable beta-TCP/Zn−Mg biocomposite [J]. Materials Research Express, 2019, 6: 0865i1.

[31] WANG Xiang, NIE Qi-dong, MA Xu-liang, FAN Jin-long, YAN Ting-liang LI Xin-lin. Microstructure and properties of co-continuous (β-TCP+MgO)/Zn−Mg composite fabricated by suction exsorption for biomedical applications [J]. Transactions of Nonferrous Metals Society of China, 2017, 27: 1996−2006.

[32] MIAO X G, LIM W K, HUANG X, CHEN Y. Preparation and characterization of interpenetrating phased TCP/HA/PLGA composites [J]. Materials Letters, 2005, 59: 4000−4005.

[33] WANG Xiang, NIE Qi-dong, LI Jing-tao, MA Xu-liang, LI Xin-lin. Microstructure and properties of interpenetrating (HA+β-TCP)/Mg−3Zn composites fabricated by suction casting [J]. Rare Metal Materials and Engineering, 2018, 47(10): 3080−3087. (in Chinese)

[34] DOROZHKIN S V. Biphasic, triphasic and multiphasic calcium orthophosphates [J]. Acta Biomaterialia, 2012, 8: 963−977.

[35] MOUSSA M E, MOHAMED H I, WALY M A, AL-GANAINY G S, AHMED A B, TALAAT M S. Comparison study of Sn and Bi addition on microstructure and bio-degradation rate of as-cast Mg−4wt.%Zn alloy without and with Ca−P coating [J]. Journal of Alloys and Compounds, 2019, 792: 1239−1247.

[36] WANG Xiang, LI Jing-tao, XIE Ming-yu, QU Li-jie, ZHANG Peng, LI Xin-lin. Structure, mechanical property and corrosion behaviors of (HA+β-TCP)/Mg−5Sn composite with interpenetrating networks [J]. Materials Science and Engineering C, 2015, 56: 386−392.

[37] WANG Xiang, DONG Li-hua, LI Jing-tao, LI Xin-lin, MA Xu-liang, ZHENG Yu-feng. Microstructure, mechanical property and corrosion behavior of interpenetrating (HA+β-TCP)/MgCa composite fabricated by suction casting [J]. Materials Science and Engineering C, 2013, 33: 4266−4273.

[38] WANG Xiang, DONG Li-hua, MA Xu-liang, ZHENG Yu-feng. Microstructure, mechanical property and corrosion behaviors of interpenetrating C/Mg−Zn−Mn composite fabricated by suction casting [J]. Materials Science and Engineering C, 2013, 33: 618−625.

[39] ASTM-G31—72. Standard practice for laboratory immersion corrosion testing of metals. Annual Book of Standards, ASTM2004 [S].

[40] PINA S, VIEIRA S I, TORRES P M C, GOETZ-NEUNHOEFFER F, NEUBAUER J, da CRUZ E SILVA O A B, da CRUZ E SILVA E F, FERREIRA J M F. In vitro

performance assessment of new brushite-forming Zn- and ZnSr-substituted β-TCP bone cements [J]. Journal of Biomedical Materials Research (Part B): Applied Biomaterials, 2010, 94: 414−420.

[41] HANIF M H M, LEE M G, MOHAMAD H M, KASIM S R. Effect of magnesium to the properties of sintered biphasic calcium phosphate (BCP) for bone regeneration [C]//Proceedings of the 3rd International Postgraduate Conference on Materials, Minerals & Polymer (MAMIP). Malaysia, 2019.

[42] DEZFULI S N, HUAN Zhi-guang, MOL A, LEEFLANG S, CHANG Jiang, ZHOU Jie. Advanced bredigite-containing magnesium-matrix composites for biodegradable bone implant applications [J]. Materials Science and Engineering C, 2017, 79: 647−660.

[43] LU Yuan, YANG Jian-feng, LU Wei-zhong, LIU Rong-zhen, QIAO Guan-jun, BAO Chong-gao. The mechanical properties of co-continuous Si_3N_4/Al composites manufactured by squeeze casting. Materials Science and Engineering A, 2010, 527: 6289−6299.

[44] BAKHSHESHI-RAD H R, HAMZAH E, LOW H T, CHO M H, KASIRI-ASGARANI M, FARAHANY S, MOSTAFA A AND MEDRAJ M. Thermal characteristics, mechanical properties, in vitro degradation and cytotoxicity of novel biodegradable Zn−Al−Mg and Zn−Al−Mg−xBi alloys [J]. Acta Metallurgica Sinica (English Letters), 2017, 30: 201−211.

[45] CHENG J, LIU B, WU Y H, ZHENG Y F. Comparative invitro study on pure metals (Fe, Mn, Mg, Zn and W) as biodegradable metals [J]. Journal of Materials Science and Technology, 2013, 29: 619−627.

[46] SHEN Chao, LIU Xi-wei, FAN Bo, LAN Ping-heng, ZHOU Fei-yu, LI Xiao-kang, WANG Hai-liang, XIAO Xin, LI Li, ZHAO Sheng, GUO Zheng, PU Zhong-jie, ZHENG Yu-feng. Mechanical properties, in vitro degradation behavior, hemocompatibility and cytotoxicity evaluation of Zn−1.2Mg alloy for biodegradable implants [J]. RSC Advances, 2016, 6: 86410−86419.

[47] TANG Zi-bo, NIU Jia-lin, HUANG Hua, ZHANG Hua, PEI Jia, OU Jing-min, YUAN Guang-yin. Potential biodegradable Zn−Cu binary alloys developed for cardiovascular implant applications [J]. Journal of the Mechanical Behavior of Biomedical Materials, 2017, 72: 182−191.

[48] FERRANDO W A. Review of corrosion and corrosion control of magnesium alloys and composites [J]. Journal of Materials Engineering, 1989, 11: 299−313.

[49] ASTM F756 — 08. Stand practice for assessment of hemolytic properties of materials. Annual Book of Standards, ASTM 2008 [S].

真空吸渗技术制备生物可降解(HA+β-TCP)/Zn−3Sn相互连续复合材料的显微组织和性能

颜廷亮，王 香，范金龙，聂其东

哈尔滨工程大学 超轻材料与表面技术教育部重点实验室，哈尔滨 150001

摘 要：利用真空吸渗技术制备(HA+β-TCP)/Zn−3Sn 相互连续复合材料。采用扫描电镜、X 射线衍射仪(XRD)、力学性能测试、电化学实验、浸泡实验和紫外分光光度计分别研究复合材料的显微组织、力学性能、腐蚀行为和溶血率。研究结果表明，Zn−3Sn 合金渗透到多孔 HA+β-TCP 骨架中形成致密的(HA+β-TCP)/Zn−3Sn 相互连续复合材料，Zn−3Sn 合金和 HA+β-TCP 骨架之间未出现反应层。复合材料的压缩强度约为 Zn−3Sn 合金块体的 3/4。复合材料在模拟体液中的腐蚀速率略高于 Zn−3Sn 合金块体的，表面腐蚀产物主要是 $Zn(OH)_2$。复合材料的溶血率低于 Zn−3Sn 合金块体的，具有较好的血液相容性。

关键词：(HA+β-TCP)/Zn−3Sn 相互连续复合材料；显微组织；力学性能；腐蚀行为；溶血率

(Edited by Wei-ping CHEN)